Highly Controllable Hierarchically Porous Ag/Ag_2S Heterostructure by Cation Exchange for Efficient Hydrogen Evolution

Huajie Xu, Xiaoxiao Niu, Zhuangzhuang Liu, Mingzi Sun, Zhaodi Liu, Zhimei Tian, Xiaoxia Wu, Bolong Huang, Yu Tang*, and Chun-Hua Yan**

H. Xu, X. Wu, Prof. Y. Tang, Prof. C.-H. Yan
State Key Laboratory of Applied Organic Chemistry, Key Laboratory of Nonferrous Metal Chemistry and Resources Utilization of Gansu Province, College of Chemistry and Chemical Engineering, Lanzhou University, Lanzhou 730000, China.
Email: tangyu@lzu.edu.cn; yan@lzu.edu.cn.

H. Xu, X. Niu, Z. Liu, Z. Liu, Z. Tian
School of Chemical and Material Engineering, Fuyang Normal University, Fuyang 236037 China.

M. Sun, Prof. B. Huang
Department of Applied Biology and Chemical Technology, The Hong Kong Polytechnic University, Hung Hum, Kowloon, Hong Kong SAR, China.
Email: bhuang@polyu.edu.hk

Keywords: Nonequivalent cation exchange, Hierarchically porous heterostructure, Metal-organic framework, Vacancies and lattice strain, Electrocatalyst

Establishing the hierarchical porous architectures has been considered to be the most efficient approach to realize the efficient mass diffusion and large exposed active sites of designed micro/nanomaterial catalysts for hydrogen evolution reactions (HER). In this work, the nonequivalent cation exchange strategy is developed to fabricate the hierarchically porous Ag/Ag_2S heterostructure based on the rapid cation exchange by the metal-organic framework (MOF)-derived CoS. The as-prepared Ag/Ag_2S inherits the original three-dimensional (3D) hollow morphology of CoS with porous nature, possessing abundant S-vacancies and lattice strain simultaneously due to the coordination loss and in-situ epitaxial growth of metallic Ag on the surface. Owing to the optimizations of lattice and electronic structures, the unique hierarchically porous Ag/Ag_2S heterostructure exhibits superior catalytic performance than previously reported catalysts derived from MOF. Theoretical calculations have confirmed that the co-existence of Ag cluster and sulfur vacancies activates the interfacial defective region to boost the HER process. The binding strength of the proton and energetic trend of HER has been

optimized with the formation of Ag/Ag_2S heterostructure, which guarantees the efficient generation of H_2. This study opens a new strategy for the utilization of the nonequivalent cation exchange strategy to efficiently synthesize advanced electrocatalysts with high performances.

1. Introduction

Hierarchically porous solid-state materials have received increasing attention in chemical/electrical energy storage, separation, photovoltaics, biomedicine sciences as well as catalysis, where the diverse compositions and porosity with abundant active sites provide large surface area to improve the efficiency, capacity and reaction kinetics.[1-3] Rational pore structure and appropriate pore size have been proved to be effective strategies for shortening the diffusion path length and reducing the diffusion constraints for their specific catalytic applications.[4,5] Therefore, the fabrication of connected hierarchically porous channels generally helps to provide a smooth transport path and improve the accessibility of active sites with long catalytic lifetimes and slow deactivation rates.[6,7] Unfortunately, most conventional synthetic strategies result in the formation of narrow pore channels (< 10 nm), causing diffusional limitations, thereby reducing the accessibility of catalytic active sites.[8, 9] Therefore, it is highly desirable to develop a new strategy for fabricating hierarchically macro-mesopores structure in interconnected porous frameworks with efficient mass transport and sufficiently exposed active surfaces.

As a template material, metal-organic frameworks (MOFs) have been widely studied in the development of novel advanced porous nanomaterials.[10, 11] Due to unique thermal and chemical instabilities, MOFs can be easily converted into metal oxides, sulfides, selenides and carbon materials.[12-15] In the processes of transformation, MOFs-derived materials can inherit their original morphologies and alleviate overgrowth and agglomeration of metal-containing clusters.[16,17] Furthermore, cation exchange (CE) reactions represent a straightforward, facile,

and effective approach to modify the properties of semiconductor nanocrystal phases by regulating metal species, ionic radius, and solvation energy of the entering and exiting cations.[18-20] In particular, the modulation of nonequivalent cation exchange usually induces the changes of charge balance, coordination mode, and local electric field by competing between metal ions and ligands.[21-24] In this exchange process, as long as the interfacial ionic transports properties and the local electric field of semiconductors are appropriately adjusted, the hierarchically macro-mesopores structure with a large number of oxygen/sulfur vacancies can be highly controllable.[25, 26] Therefore, the nonequivalent cation exchange modulation of MOFs-derived nanocrystal materials will be a facile and efficient strategy to create hierarchical porosity filled with highly active sites.

Engineering sulfur vacancies (S-vacancies) and strain have been proven to be a robust strategy in regulating the surface electronic structure for boosting hydrogen evolution reaction (HER).[27-31] However, on the one hand, most methods to generate S-vacancies involve plasma exposure or annealing treatment of the reduction atmosphere, and the S-vacancies concentration generated by these operations is not easily controlled or low.[32, 33] On the other hand, most of the lattice strain was induced by physically bending or stretching and deforming the supporting substrate, thus the control degree of strain magnitude is limited and suffers from the difficulty of scaling up.[34-36] Recent studies have also shown that the introduction of strain on the heterostructure interface can not only tailor the electronic structure but also promote the formation of S-vacancies as active sites for the HER.[37-39] Therefore, exploring strain and S-vacancies engineering promotes the utilization of active sites. However, manipulating these two parameters of strain and S-vacancies simultaneously for boosting HER activity is still extremely challenging.

Herein, we have developed a delicate and versatile nonequivalent cation exchange strategy for the rational design and controllable synthesis of porous Ag/Ag_2S heterostructure with lattice strain and S-vacancies, in which pore sizes and pore volumes can be facilely tuned. The experimental procedures involved in the synthesis are summarized in **Figure 1a**. MOF-derived CoS with Co^{2+} and Co^{3+} metal nodes was selected as the original microporous precursor (Figure S1). Nonequivalent cation exchange reactions are realized between $Co^{2+/3+}$ ions and Ag^+ ions to change the original coordination mode of Co nodes, and completely reassemble coordination bonds of Ag/Ag_2S heterostructure with a large number of lattice strain and S-vacancy sites. In addition, Ag^+ as a modulator to control nucleation and crystal growth rate by competing with CoS linkers was capable of adjusting the pore size from micropore to macropore, achieving efficient mass transport as well as produce sufficiently exposed active surface in the porous frameworks. The as-prepared large-pore Ag/Ag_2S heterostructure material shows excellent catalytic efficiency for HER with the synergy of lattice strain and S-vacancy sites. Theoretical calculations have revealed that the introduction of the electron-rich Ag cluster on the surface not only leads to increased strain but also optimizes the binding strength of the proton. The existence of abundant vacancies and surface Ag clusters lead to improved electron transfer efficiency from catalysts to proton for realizing efficient HER. More importantly, this facile and effective synthesis strategy is able to guide the design of new types of hierarchically macro-mesopores catalysts.

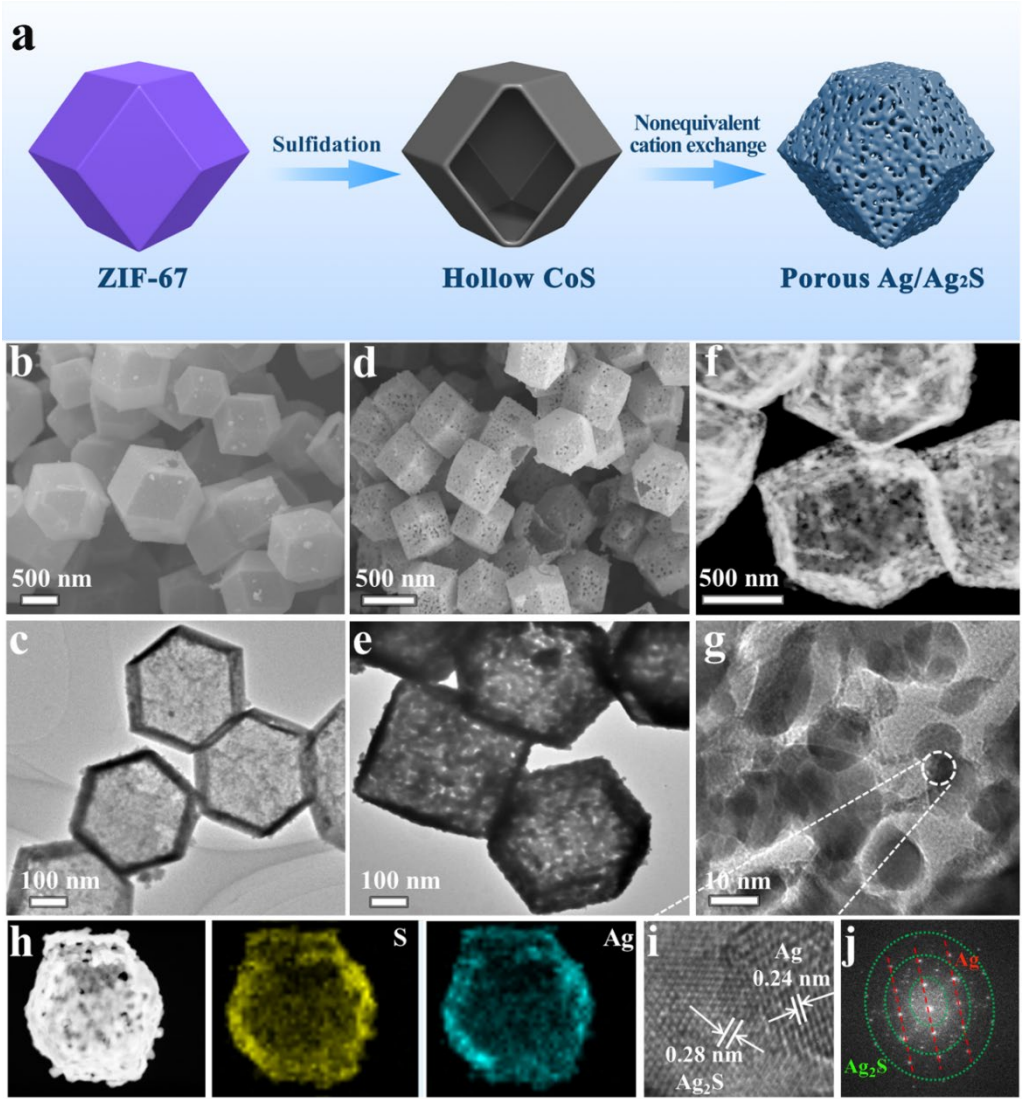

Figure 1. (a) Illustration of the fabrication process of porous Ag/Ag_2S. SEM and TEM images for precursor CoS (b, c) and for Ag/Ag_2S (d, e). The HAADF-STEM image (f) and HRTEM images (g, i) and corresponding SAED pattern (j) for the Ag/Ag_2S. (h) Elemental mapping images of Ag/Ag_2S.

2. Results and Discussion

2.1. Construction and analysis of porous Ag/Ag_2S heterostructure

According to the schematic illustration in Figure 1a, uniform hollow CoS nanocages were first synthesized by using a modified Kirkendall process of polyhedral nanocrystal ZIF-67 as the initial precursor for porous Ag/Ag_2S heterostructure preparation. Some typical scanning electron microscopy (SEM) and transmission electron microscopy (TEM) images for ZIF-67 and ZIF-67-Derived CoS can be found in Figure 1b,c and Figure S2. Obviously, due to the

gradual transfer of sulfur ions from thioacetamide onto the surface of the self-sacrificing ZIF-67 template, the formed hollow CoS well maintains the initial morphology. Then, the resultant MOF-derived CoS served as a precursor and mixed with $AgNO_3$ (Ag source) to synthesize the three-dimensional (3D) porous Ag/Ag_2S via the nonequivalent cationic exchange method. Importantly, the attractive hierarchical hollow structure possesses interconnected macro-/meso-/micropores with substantial exposed contact area, which will be beneficial to achieve efficient mass transport and reactant diffusion during the electrochemical reaction process. The morphology was characterized by SEM and TEM. The SEM image (Figure 1d) shows that Ag/Ag_2S not only retains the complete hollow dodecahedral shape but also displays the hierarchical porosity on the surface due to the nonequivalent cationic exchange reaction. Therefore, such a structure has guaranteed the exposure of active sites and fast release of gas molecules, thereby facilitating the mass transport and further promote the HER performances. TEM and high angle annular dark-field scanning transmission electron microscopy (HAADF-STEM) images (Figure 1e,f,g) display an irregular porous distribution with an average size of ~20 nm and further confirm the prepared Ag/Ag_2S has a highly porous topography. In Figure 1h, the elemental mappings of Ag and S in a single polyhedral nanocrystal show that Ag and S elements are uniformly distributed in the 3D porous skeleton. The high-resolution TEM (HRTEM) image (Figure 1i) of Ag/Ag_2S displays the lattice fringe spacings of 0.28 and 0.24 nm, representing the interplanar distance of (-112) and (111) of hexagonal Ag_2S and cubic Ag, respectively. The corresponding fast Fourier transform (FFT) pattern based on the HRTEM image also confirms the formation of mixing phase by Ag_2S (green) and Ag (red) in the material (Figure 1j), in which a spherical metallic Ag has epitaxially grown at Ag_2S cluster forming a uniform Ag/Ag_2S heterostructure. Furthermore, the atomic ratio of Ag/S measured by EDX spectrum was about 2.3:1 (Figure S3), which was much larger than the stoichiometric ratio of 2:1 for the phase-pure Ag_2S. This further confirmed the formation of metallic Ag on the surface of Ag_2S. Meanwhile, there was almost no cobalt element in the EDX spectrum, indicating that

complete ion exchange between Ag and Co ions, which was also consistent with the absence of photoelectrons signal of Co 2p in the XPS spectrum for the obtained Ag/Ag_2S (Figure S4). The crystallographic structure and surface information of the porous Ag/Ag_2S heterostructure were further examined by X-ray powder diffraction (XRD) and X-ray photoelectron spectroscopy (XPS) measurements. The XRD analysis results are shown in Figure S5, in which the unmarked diffraction peaks can be assigned to monoclinic Ag_2S (JCPDS card No. 77-0072), and the corresponding peaks of face-centered cubic Ag (JCPDS card No. 87-0720) are marked by asterisks. The XRD results have proved that Ag/Ag_2S heterostructure hybrid materials have been successfully obtained by the cation exchange method.

Then, the XPS spectra were performed to investigate surface information of the Ag/Ag_2S hybrid as shown in Figure S6. The peaks at 368.15 and 374.15 eV in the Ag 3d photoelectron spectrum correspond to the binding energies of Ag $3d_{5/2}$ and Ag $3d_{3/2}$ of Ag^+ ions, respectively, whereas the peaks at 368.55 and 374.45 eV are attributed to the binding energies of Ag $3d_{5/2}$ and Ag $3d_{3/2}$ of the metallic Ag^0. Therefore, the co-existence of Ag^+ ions and metallic state (Ag^0) in the Ag/Ag_2S heterostructure was confirmed again.

2.2. Pore structure control

The morphological control and formation processes of the hierarchical porous heterostructured Ag/Ag_2S are further revealed. Converting the MOF-derived hollow CoS into porous Ag/Ag_2S hybrid materials could be realized by precisely controlling the exchange process between Co^{2+} and Ag^+ (**Figure 2a**). The hollow CoS nanocage was obtained using ZIF-67 as the self-sacrificing template, and then the cation exchange reaction between CoS particles with Ag^+ was performed through a solvothermal reaction. Compared with CoS (4.0×10^{-21}, 18 °C), the K_{sp} of Ag_2S (1.0×10^{-49}, 18 °C) is very small, so the nonequivalent cation-exchange reaction will naturally occur between Co^{2+} and monovalent Ag^+ with additional $AgNO_3$. However, the

degree and speed of cation exchange were the key factors to precisely regulate the pore size of nanomaterials. The SEM image of MOF-derived CoS shows the solid nature and smooth surface (Figure 2b). In the presence of Ag^{+}, the weak Co-S bonds break and form Ag-S bonds synchronously, which leads to the mismatch of chemical valence between $Co^{2+/3+}$ and Ag^{+}, and then changes the coordination mode, forming the porous morphology with abundant defects. Interestingly, the pore sizes have been increased with initial Ag^{+} concentration from 5 to 30 mM, which can be clearly observed from the SEM images (Figure 2c-g). Subsequently, detailed pore size distribution was also investigated (Figure 2h and Figure S7), which clearly showed a steadily increased pore size from 3 to 50 nm by varying initial Ag^{+} concentration. Therefore, the pore size evolution of the porous composite was highly Ag^{+}-concentration dependent, which indicated that Ag^{+} was introduced as a modulator not only controls the crystal growth and nucleation rate by competing with CoS linkers but also induces the chemical valence mismatch to form defective pore regions.

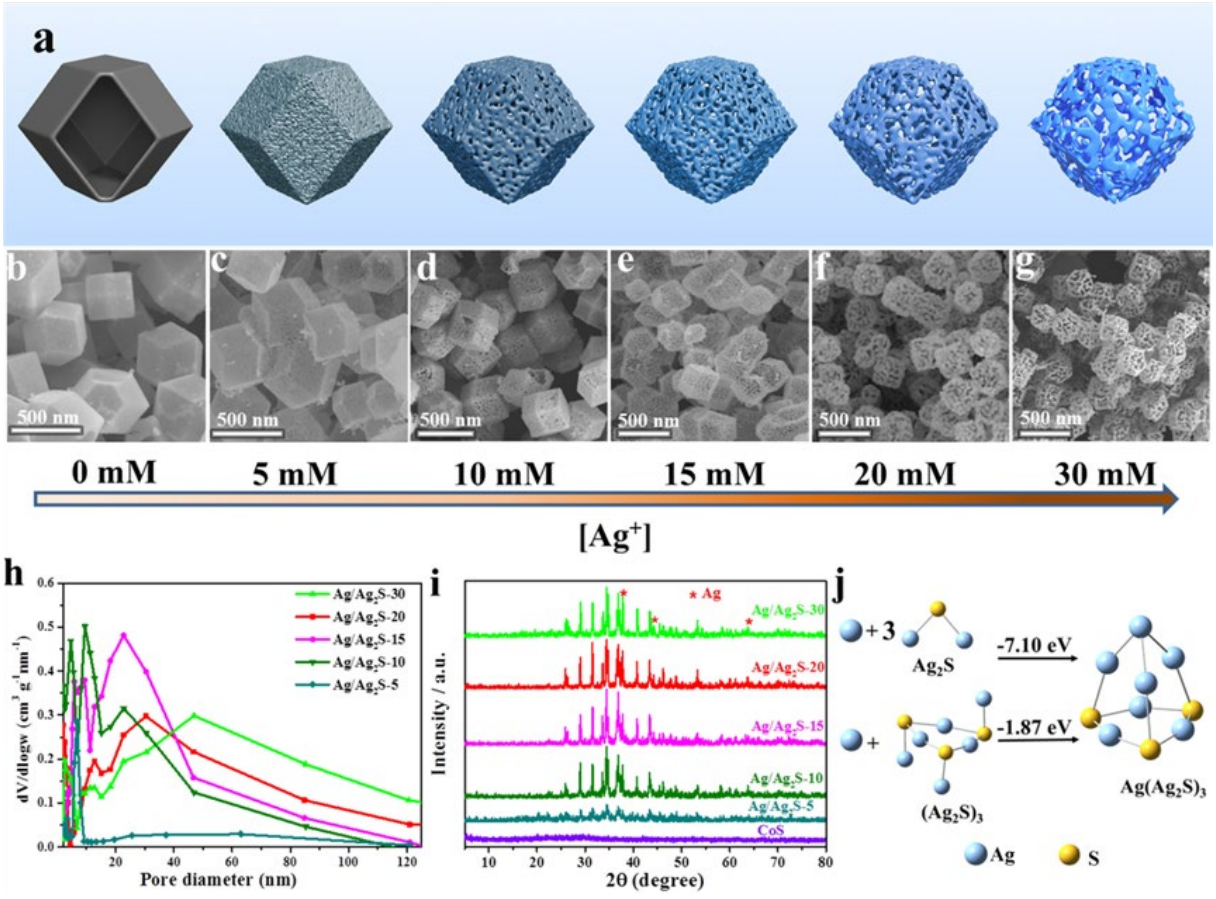

Figure 2. (a) Schematic illustration of the formation process of a hierarchically macro-/mesoporous Ag/Ag_2S. SEM images of Ag/Ag_2S obtained by adding different initial Ag^+ concentrations into the CoS solution. (b) [Ag^+] = 0, (c) [Ag^+] = 5 mM, (d) [Ag^+] = 10 mM, (e) [Ag^+] = 15 mM, (f) [Ag^+] = 20 mM, (g) [Ag^+] = 30 mM. (h) Pore size distributions calculated from the N_2 adsorption isotherms of Ag/Ag_2S. (i) XRD patterns of CoS and Ag/Ag_2S. (j) The formation processes of $Ag(Ag_2S)_3$ cluster on the basis of the Ag/S ratio of about 2.3. Blue balls =Ag and Yellow balls = S.

Then, we further studied the effects of initial Ag^+ concentrations on the composition of the porous materials. When the reaction concentration of Ag^+ was 5 mM, the hollow CoS partially exchanges with Ag^+, resulting in the co-existence of CoS and Ag_2S in the composite material, which are confirmed by the presence of Co and Ag signals in the elemental mapping and EDX results (Figure S8). However, when the Ag^+ concentration was further increased to 10 mM, the CoS was fully transformed into Ag_xS, which can be deduced from disappeared Co signals in EDX (Figure S9a). Noticeably, with different initial Ag^+ concentrations, Ag-substituted CoS nanoboxes exhibited different ratios of Ag and S atoms, and the corresponding Ag/S atomic ratios of 15, 20 and 30 mM silver nitrate concentrations were 2.14, 2.35, and 2.28 (Figure S9b-d), respectively, and the Ag/S atomic ratios trend was also consistent with the ICP-AES measurements (Table S1-S2). The increasing Ag/S atomic ratio indicates that the high concentration of Ag^+ has a higher reactivity with sulfur, and rapidly nonequivalent ion exchange with cobalt ions, and then the interfacial reconstruction and sulphur coordination mismatch induce a large number of sulfur vacancies and other defects, promoting the in-situ reduction of Ag_2S to form metallic Ag^0 species upon mild heating. Thus, some metallic Ag^0 incorporated the crystal system of Ag_2S, forming Ag_xS phase ($x \geqq 2$), which further confirms the formation of the intimate Ag/Ag_2S heterostructure with a tight connection, which is also consistent with the observation of STEM images mentioned above (Figure 1i). In addition, the formation process of Ag/Ag_2S heterostructure can also be confirmed from the gradually increasing diffraction peaks of metallic Ag in XRD (Figure 2i). However, although the amount of metallic Ag^0 increases gradually with the increase of $AgNO_3$ solution concentration and the prolonged

immersion time (Figure S10), the Ag:S ratio reach a limit of about 2.41 with similar morphology (Figure S11), which is attributed to the finite reducing ability of sulfur.

To further elucidate the tendency to form stable the Ag/S ratio of about 2.3 in the Ag/Ag_2S heterostructure, we carried out a hybrid density functional theory (DFT) method to build the $Ag(Ag_2S)_3$ model on the basis of the Ag/S ratio (see calculation details in the Supporting Information). The formation of $Ag(Ag_2S)_3$ can be viewed as the combination of one Ag and three Ag_2S, or the combination of one Ag and one $(Ag_2S)_3$. The formation processes of the $Ag(Ag_2S)_3$ are displayed in Figure 2j, both of which are exothermic processes, releasing -7.10 and -1.87 eV respectively, which is also consistent with the previous theoretical studies.[40] Therefore, the calculation results show that the formation process of Ag/Ag_2S heterostructure is energetically favorable.

2.3. Electrochemical performances

Inspired by the unique porous heterostructure and expected composition, the electrochemical HER activity of Ag/Ag_2S was evaluated by a typical three-electrode cell in 0.5 M H_2SO_4 aqueous electrolyte. For comparison, the HER performance of Ag nanocrystals, the commercial Pt/C (20 wt%) and MOF-derived CoS were also measured under the same condition. As can be seen from the iR-corrected linear sweep voltammograms (LSV) in **Figure 3a**, compared to MOF-derived CoS (η_{10} = 331 mV), all Ag/Ag_2S heterostructures showed much higher HER catalytic activity, while Ag nanocrystals exhibited no measurable HER activity within the investigated potential window. Encouragingly, by adding different initial Ag^+ concentrations, the catalytic activity of obtained Ag/Ag_2S increased gradually.

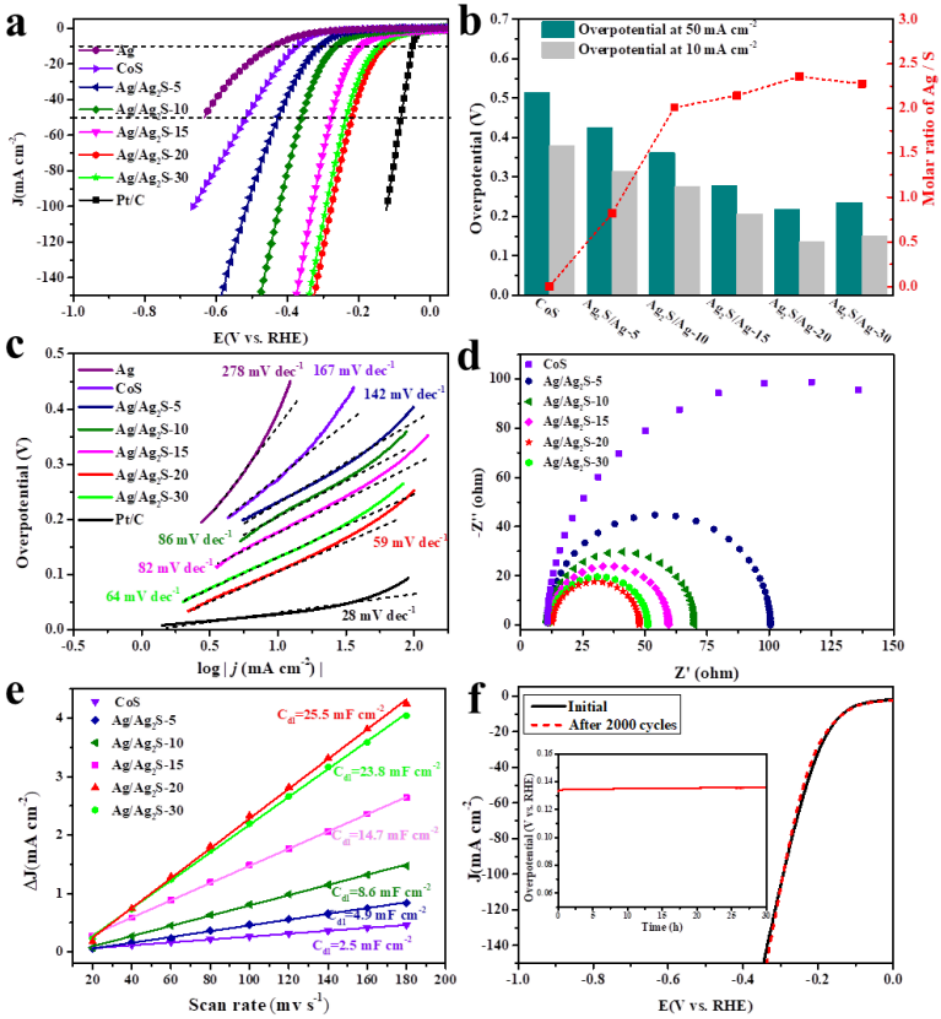

Figure 3. (a) Polarization curves of Ag, CoS, Ag/Ag_2S and Pt/C for HER. (b) The relationship between overpotential (at j = 10 (gray) and 50 (cyan) mA cm^{-2}) and Ag/S ratio. (c) Tafel slopes of Ag, CoS, Ag/Ag_2S and Pt/C. (d) The Nyquist plots of CoS and Ag/Ag_2S. (e) The plot of capacitive current density versus scan rate for CoS and Ag/Ag_2S. (f) Polarization curves for Ag/Ag_2S-20 before and after 2000 cycles (Inset: Chronopotentiometric curve for the Ag/Ag_2S-20 at 10 mA cm^{-2}).

As a result, for the Ag/Ag_2S-5, Ag/Ag_2S-10, Ag/Ag_2S-15 and Ag/Ag_2S-20 catalysts, the required overpotential values were 315, 276, 206 and 136 mV to afford the current density of -10 mA cm^{-2}, respectively. Nonetheless, when the initial Ag^+ concentration increased to 30 mM, the catalytic performance decreased with an overpotential of 149 mV for -10 mA cm^{-2}. Moreover, at a current density of -50 mA cm^{-2}, for the Ag/Ag_2S-5, Ag/Ag_2S-10, Ag/Ag_2S-15, Ag/Ag_2S-20 and Ag/Ag_2S-30 catalysts, the overpotential values were 426, 362, 279, 219 and 235 mV, respectively, which were much lower than that of CoS (515 mV). Figure 3b displays

the relationship between overpotentials at j = 10 mA cm^{-2} (gray color column) and j = 50 mA cm^{-2} (green color column) and the Ag/S atomic ratios on Ag/Ag_2S catalyst surfaces. The results showed that with the increase of the Ag/S ratios from 0.85 to 2.35, the catalytic performance for HER gradually improved, and then decreased slightly when the Ag/S atomic ratio was 2.28 for Ag/Ag_2S-30. The volcano-like change of the Ag/S atomic ratios was highly consistent with the trend of HER activity as a function of the amount of Ag, which may be due to the introduction of the more metallic Ag further activates the electroactivity of S sites at the interface. Obviously, the Ag/Ag_2S-20 was the best of them, and the overpotential of 136 mV was closer to the commercial Pt/C and comparable to the performance of the most reported non-noble metal HER catalysts (Table S3). Such excellent catalytic performance can be attributed to the unique porous Ag/Ag_2S micro/nanostructures with many lattice defects, abundant heterojunction interfaces, and fast diffusivity.

To reveal the underlying mechanism of HER activity, the Tafel plots were also investigated as shown in Figure 3c. The Ag/Ag_2S-20 displayed a smaller Tafel slope of 59 mV dec^{-1} than the pristine CoS (167 mV dec^{-1}) and other Ag/Ag_2S catalysts, indicating a faster hydrogen generation rate and higher activity, which corresponded with the polarization curve. The increasing HER reaction kinetics benefited from the synergistic effect of hollow porous Ag_2S and the in-situ formation of metallic Ag. To gain further insight into the conductivity and the charge transport capability of catalysts, electrochemical impedance spectroscopy (EIS) was also carried out (Figure 3d). As seen from the Nyquist plots, the order of the charge transfer resistance was Ag/Ag_2S-20 < Ag/Ag_2S-30 < Ag/Ag_2S-15 < Ag/Ag_2S-10 < Ag/Ag_2S-5 < CoS, the result mainly attributed to metallic Ag coupled with Ag_2S matrix constructing hetero-interface acted as an excellent electron conductor to improve the electron transfer ability. In addition, the intrinsic activity of catalysts toward HER was probed by the double-layer capacitance (C_{dl}) to estimate the electrochemically active surface areas (ECSA). The CV curves

of CoS and Ag/Ag_2S with different scan rates were shown in Figure S12. As presented in Figure 3e, the C_{dl} of 25.5 mF cm^{-2} for Ag/Ag_2S-20 was much higher than those for CoS (2.5 mF cm^{-2}), Ag/Ag_2S-5 (4.9 mF cm^{-2}), Ag/Ag_2S-10 (8.6 mF cm^{-2}) and Ag/Ag_2S-15 (14.7 mF cm^{-2}). The higher C_{dl} value for the Ag/Ag_2S-20 catalyst means more potential active sites for HER. This result indicates that the non-equivalent cation exchange strategy constructs porous Ag/Ag_2S heterostructure discrete domains, which is potentially rich in lattice defects and lattice strain, thus contributing to more accessible active sites.

For most 3D porous materials, stability is a key factor of note for catalytic performance, as exposure to electrolytes prone to degrade the unsupported 3D framework. Then, the operational stability of Ag/Ag_2S was also verified by long-term chronopotentiometry at an applied current density of 10 mA cm^{-2} and CV scanning 2000 cycles. As shown in Figure 3f, the HER catalytic activity of Ag/Ag_2S-20 can maintain at least 30 h and the negligible difference could be observed from the LSV curve after 2000 cycles. Moreover, the interconnected 3D porous structure morphology can be well preserved after the long-term electrolysis (Figure S13), and no obvious metal leaching was found as revealed by ICP-AES (Table S4). The XRD pattern and Ag 3d XPS spectra after HER demonstrated almost no obvious structural and valence state changes (Figure S14-S15). Therefore, the above experimental results indicate that the hierarchically porous Ag/Ag_2S materials have excellent HER electrocatalytic activity and stability.

2.4. Structure-performance relationship

To further uncover the structure-performance relationship, the Ag 3d XPS spectrum was performed to study the formation processes of Ag/Ag_2S heterostructures. When the initial concentration of Ag^+ increased from 5 to 20 mM, as shown in **Figure 4a**, the relative spectral intensity of Ag $3d_{5/2}$ and Ag $3d_{3/2}$ showed that the ratio of the metallic Ag^0 increased

significantly. In particular, there was also a large shift in the binding energy, indicating an increase in electron transfer due to the coulomb or polaronic interactions between Ag particles and the Ag_2S matrix. More importantly, the volcano-like change of the metallic Ag molar ratio is in good agreement with the trends of HER activity as a function of the amount of Ag, suggesting that in-situ conversion of appropriate metallic Ag can regulate the surface electronic coupling and the binding energy, thus facilitating the adsorption of hydronium ion in aqueous solution. Meanwhile, as there are multiple nanojunction (Ag/Ag_2S) interfaces and metallic Ag is located at the edge of the multi-component heteronanostructures, which promote the formation of highly exposed Ag^0 sites and high-energy Ag/Ag_2S interfaces. In addition, the heterostructural cooperation between Ag^0 and adjacent Ag^+ Lewis acid sites would also create unique local electrostatic fields at the interfaces. Such structural features with ultra-fine metallic Ag homogeneously dispersed on the surface of Ag_2S clusters generating high energy sites to significantly boost the catalytic performance.

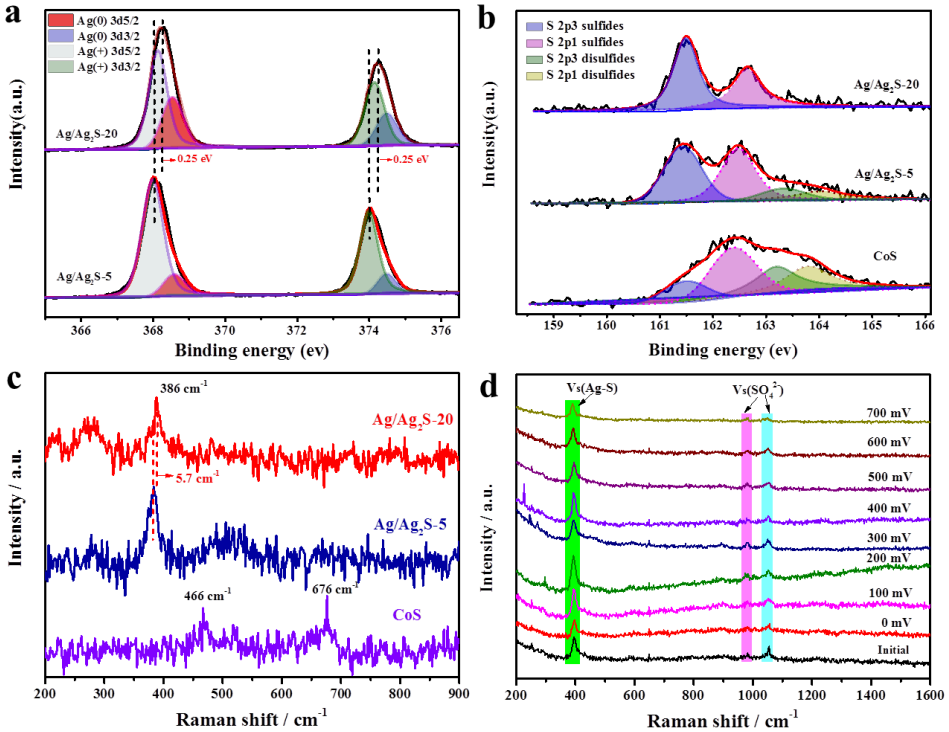

Figure 4. (a) The XPS spectra of Ag 3d for Ag/Ag_2S-5 and Ag/Ag_2S-20. (b) The XPS spectra of S 2p. (c) Raman spectra for CoS, Ag/Ag_2S-5 and Ag/Ag_2S-20. (d) In situ Raman spectra of HER on Ag/Ag_2S-20 in a 0.5 M H_2SO_4 solution.

A considerable amount of S-vacancies derived from lattice mismatch can create more active sites and decrease the free energy of hydrogen adsorption (ΔG_H) for HER. The substitution of Ag^+ to $Co^{2+/3+}$ sites from nonequivalent cationic exchange reaction, charge unbalance brings about the lattice mismatch and induce the formation of S-vacancies at the vertical interface. The formation of S-vacancies can be monitored by S 2p XPS, Raman spectra, and electron spin resonance (ESR) spectra. S 2p XPS (Figure 4b) of MOF-derived CoS shows two pairs of doublets centred at 163.2 &163.8 eV and 161.5 & 162.4 eV, which are corresponding to S $2p_{3/2}$ and S $2p_{1/2}$ bands of disulfide and S^{2-} species, respectively. Upon exposure to 5 mM of Ag^+ solution, the peak intensities of S 2p disulfide at around 163.2 and 163.8 eV decreased significantly, indicating that S-S bonds were partially eliminated and transformed into Ag_2S during Ag^+ incorporation. However, when the Ag^+ concentration further increased to 20 mM, there is only one pair of the doublet with binding energies of 161.4 & 162.5 eV corresponding to S $2p_{3/2}$ and S $2p_{1/2}$, indicating the existence of only S^{2-} state of S element. The disappearance of the S-S bond signal peak was attributed to CoS being completely converted to Ag_2S in a higher concentration silver nitrate solution.

The transformation was further studied using Raman spectroscopy, as shown in Figure 4c. The Raman spectrum of MOF-derived CoS exhibited two peaks at 466 and 676 cm^{-1}, corresponding to the S-S stretching and Co-S vibrational mode, respectively. With the constant addition of Ag^+ ions into CoS, the initial peak strength decreased or disappeared. This was due to the fact that the sulfur atoms in CoS gradually combine with Ag^+ competitively, resulting in the disulfide bonds fracture in CoS and the formation of Ag_2S with a newly formed vibrational peak at 386 cm^{-1}, which was consistent with XPS results. Notably, the Ag-S vibration peak has a redshift of 5.7 cm^{-1} in Ag/Ag_2S, which is attributed to the formation of lattice defects and distortion caused by coordination mismatch environment, especially, the formation of a large

number of S-vacancies induced by S-S bond fracture. In situ Raman spectra were also used to investigate the structural changes of the catalysts under operando conditions (Figure 4d), and the varying Ag-S vibration peak strength, indicating that the introduction of S-vacancies may lead to such structural disorder.

Furthermore, the ESR spectra measurements were performed to provide strong evidence for exploring the generation and variation of S-vacancies,[41, 42] the enhanced vacancy-related ESR signal indicated the defect-rich nature on the Ag/Ag_2S interface (Figure S16). In addition, with the increase of Ag/Ag_2S aperture, the ESR peak intensity increased gradually, and these deficiencies may act as the anchoring sites for metallic Ag with uniform dispersion. This result indicates the density of S-vacancies depends crucially on the in-situ epitaxial growth of metallic Ag as well as the pore size, and formation of the metallic Ag may favor the generation of more S-vacancies.

Lattice strain induced by epitaxial growth of Ag/Ag_2S heterostructures also plays a dominant role in boosting the HER activity. As schematically illustrated in **Figure 5a**, metallic Ag uniformly dispersed on the surface of Ag_2S clusters and coupled with Ag_2S matrix can act as a good electron conductor. In the unique 3D porous Ag/Ag_2S heterostructure, in-situ epitaxial growth metallic Ag on the Ag_2S surface to form the stacked heterogeneous interfaces cause the lateral confinement imposed by twin boundaries. The Ag overlayers could only relax along the direction normal to the surface to generate a corrugated structure with compressive strain (Figure 5b). Such a corrugated structure can be well maintained even after the catalytic reaction (Figure S17). In the Raman spectra of Figure 4c, a redshift of 5.7 cm^{-1} for the Ag-S vibration peak observed here is much larger than that obtained by previous strain methods,[29,30] indicating the presence of considerable strain in the porous Ag/Ag_2S heterostructure.

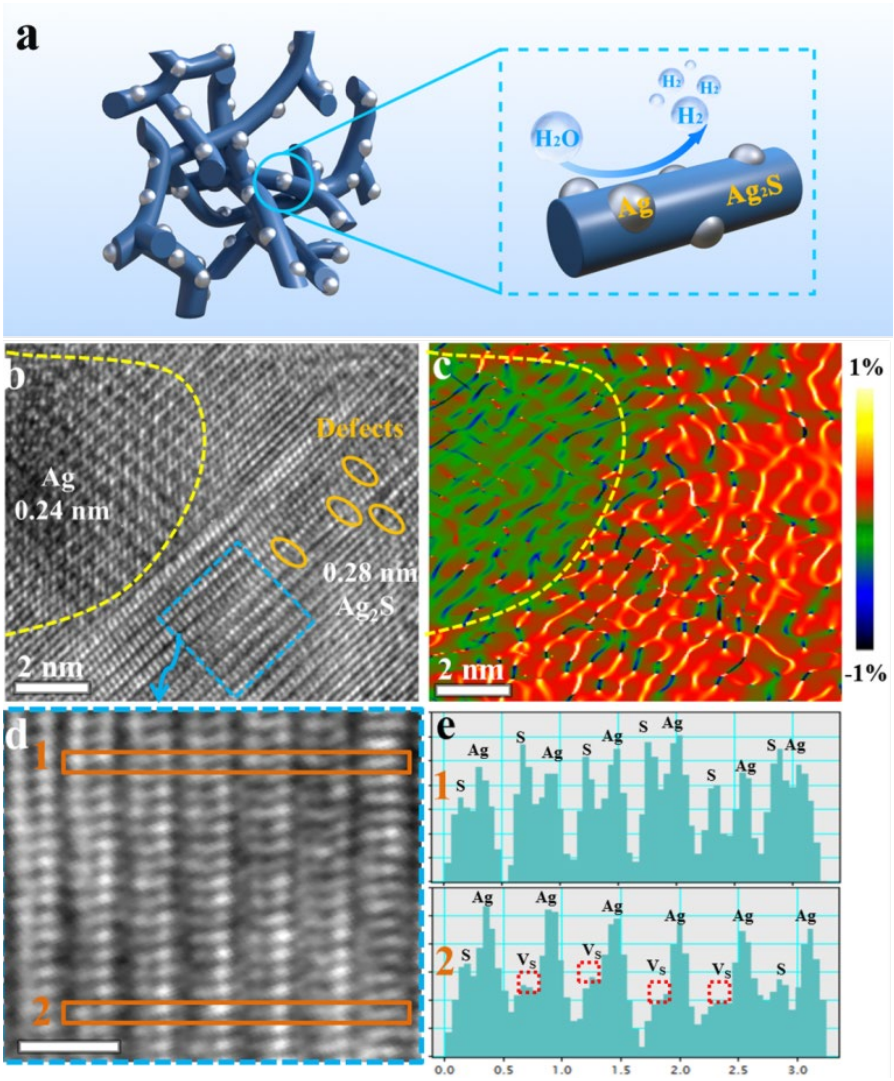

Figure 5. (a) Schematic illustration of Ag/Ag_2S heterostructures, demonstrating the role of metallic Ag and Ag_2S clusters. (b) Atomic-resolution HRTEM image of Ag/Ag_2S-20. (c) The strain tensor map generated from the HRTEM image using geometric phase analysis. (d) The magnified atomic-resolution HAADF-STEM image of Ag/Ag_2S-20. (e) Comparison of intensity profiles along the selected rectangular regions suggests the missed surface S atoms in Ag/Ag_2S-20. Scale bar, 0.5 nm.

In order to reveal the in-plane 3D strain state, the geometric phase analysis (GPA) strain maps in the Ag/Ag_2S were obtained and the vertical strain (3yy) map was shown in Figure 5c. The strain maps result clearly show that the Ag/Ag_2S heterostructures are full of strong and well-regulated lattice strain, and the strain tends to aggravate the lattice distortion and create more vacancy sites, which has been confirmed by previous studies.[33, 43] In the Ag/Ag_2S crystal lattice structure, the interfacial feature of strong lattice distortion, as well as the defects induced by

missing atoms, can be clearly observed (Figure 5d).In addition, the intensity profiles along the selected rectangular regions also suggest the missed surface atoms in Ag/Ag_2S interfacial structure (Figure 5e). Due to the in-situ epitaxial growth mode, the obtained Ag/Ag_2S heterostructures inherently generate strong strain and induce more S-vacancies, thus accelerating electron and mass transport, greatly facilitating the access of active sites. Moreover, compressive strain significantly decreases activation energies of the vacancies and improves charge-carrier density and mobility contact, which contribute to better catalytic performance.[38] More importantly, the ability to readily fine-tune the pore size of the Ag/Ag_2S heterostructure by changing initial Ag^+ concentration provides a convenient way to construct lattice strains and S-vacancies simultaneously, which is crucial for optimizing the HER activity.

2.5. DFT calculations

To investigate the superior HER performances of Ag/Ag_2S heterostructure, we have further carried out the DFT calculations. To compare the electronic modulations induced by both defects and Ag clusters on the surface, we have compared the electronic distributions of pristine Ag_2S, defective Ag_2S, and Ag/Ag_2S heterostructure. Notably, the (-112) surface of pristine Ag_2S has shown a highly ordered electronic distribution, in which the surface S sites dominate the electroactivity while a small part of Ag sites also contributes to the bonding states (**Figure 6a**). With the formation of the surface sulfur defects, the electronic distributions and surface structures have been significantly perturbed, which leads to the fragmentations of the surface electroactive regions (Figure 6b). Such surface electron-rich regions are constructed by the Ag sites near defects and the surface S sites. However, for Ag/Ag_2S heterostructure, we notice that the surface Ag cluster has shown a highly electron-rich feature. With the formation of the Ag cluster on the surface, the interface region has been activated (Figure 6c). These highly electroactive interfacial regions facilitate the electron transfer from the catalyst surfaces to the proton. Then, we carried out the detailed electronic structures of the Ag/Ag_2S heterostructure

based on the projected partial density of states (PDOS) (Figure 6d). Notably, the *s,p* orbitals of S sites have occupied close positions to the Fermi level (E_F), which plays as the electron depletion center towards the protons. In comparison, the 4*d* orbitals of the surface Ag cluster and Ag_2S are different, in which 4*d* orbitals of Ag clusters show the dominant peak at E_V-3.3 eV (E_V denotes 0 eV). 4*d* orbitals of Ag_2S show a subtle downshifting of 0.4 eV at E_V-3.7 eV. From the inset, it is noted that the co-existence of surface Ag clusters and sulfur vacancies have resulted in the evident lattice distortion, supporting the intrinsic strain in Ag/Ag_2S heterostructure. Different Ag sites in Ag/Ag_2S heterostructure have shown site-dependent electronic structures (Figure 6e). From the Ag_2S to the surface Ag cluster, the 4*d* orbitals have become broaden, which supports a more electron-rich feature. The Ag sites have demonstrated a distinct electronic structure to the metallic Ag. For the Ag sites at the interfacial region of the heterostructure, we notice the expansion of 4*d* orbitals. Ag sites in the Ag clusters exhibit a similar electronic structure to the metallic Ag, supporting the experimental characterizations. On the other side, the electronic structures of electroactive S sites have also been modulated by the formation of Ag/Ag_2S heterostructure (Figure 6f). In the Ag/Ag_2S heterostructure, the S sites in the bulk Ag_2S have displayed a similar electronic structure to that in the pristine Ag_2S. However, from the bulk Ag_2S to the interface of Ag/Ag_2S heterostructure, we notice that the *s,p* orbitals have upshifted from E_V-2.2 eV to E_V-1.15 eV, supporting a significantly improved electron transfer capability towards the proton. These results confirm that the introduction of the Ag cluster further activates the electroactivity of S sites at the interface. These electroactive interfacial S sites are the key factor to improve the HER performances.

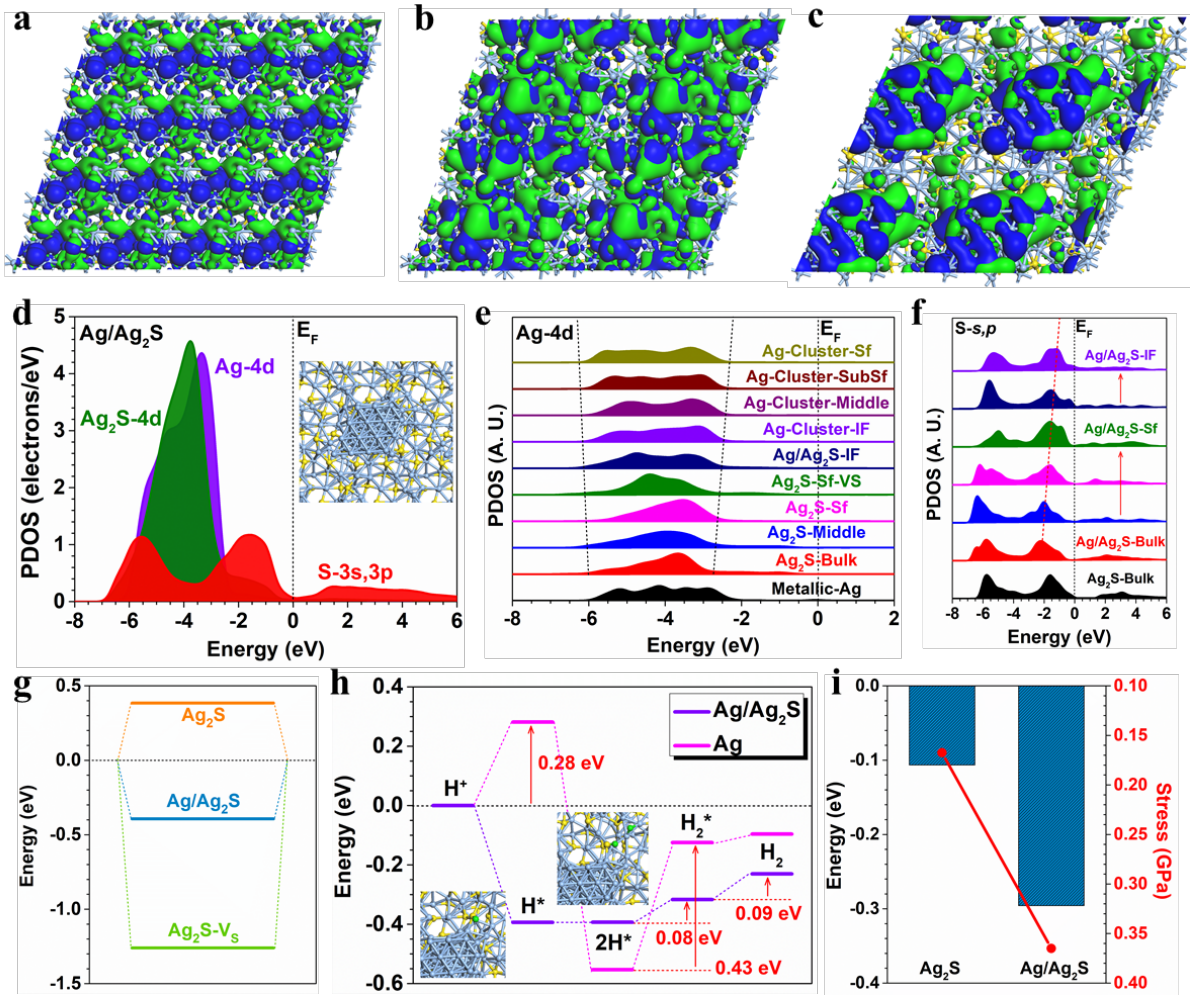

Figure 6. The 3D contour plot of electronic distribution near the Fermi level of (a) pristine Ag_2S, (b) defective Ag_2S with sulfur vacancies, and (c) Ag/Ag_2S heterostructure. (d) The PDOS of Ag/Ag_2S heterostructure. Light blue balls represent Ag atoms and yellow balls represent S atoms. (e) The site-dependent PDOS of Ag-4d in Ag/Ag_2S heterostructure. (f) The site-dependent PDOS of *s,p* orbitals of S sites in Ag/Ag_2S heterostructure. (g) The adsorption of H in pristine Ag_2S, defective Ag_2S, and Ag/Ag_2S heterostructure. (h) Energetic pathway of HER in the acidic environment on Ag/Ag_2S heterostructure. Light blue balls represent Ag atoms, yellow balls represent S atoms and green balls represent the adsorbed H atoms. (i) The formation energies of sulfur vacancies and stress in Ag_2S and Ag/Ag_2S.

Then, we consider the proton binding strength in different structures (Figure 6g). Pristine Ag_2S has shown a low preference for the proton bindings, which shows an energy cost of 0.39 eV. In comparison, the Ag/Ag_2S have shown the optimal adsorption bind strength of -0.39 eV while the defective Ag_2S shows the overbinding effect of the proton. The optimized binding energy of the proton indicates that the introduced Ag cluster facilitates the electroactivity and avoids overbinding. The HER process shows an exothermic trend with an overall energy release of -

0.23 eV (Figure 6h). From 2H* to H_2*, there is an energetic barrier of 0.08 eV. The desorption of formed H_2 also only requires an energy cost of 0.09 eV, supporting an efficient generation of H_2. All the HER process occurs near the interfacial regions, where the S sites adsorb the first proton and Ag sites near sulfur vacancies facilitate the second proton adsorption. In comparison, the HER process on the pristine Ag surface shows a large energy barrier (0.28 eV) for the initial adsorption of the proton. In addition, the formation of H_2* requires 0.43 eV energy cost, leading to a much lower HER efficiency than Ag/Ag_2S heterostructure. In the end, we have also compared the formation energies of sulfur vacancies on both pristine Ag_2S and Ag/Ag_2S heterostructure (Figure 6i). It is noted that the formation of sulfur vacancies becomes more favorable in the Ag/Ag_2S heterostructure, supporting the experimental results of abundant defects in the Ag/Ag_2S heterostructure. Moreover, the stress in Ag/Ag_2S heterostructure is also two times larger than that in pristine Ag_2S, indicating the much larger strain induced by the introduction of Ag cluster on the surface. These results confirm the co-existence of sulfur vacancies and lattice strain in the Ag/Ag_2S heterostructure in promoting the HER performances. Therefore, theoretical calculations have confirmed the engineering of the Ag/Ag_2S heterostructure significantly boosts the HER performance.

3. Conclusion

In summary, we have developed a nonequivalent cation exchange strategy for the fabrication of hierarchically porous Ag/Ag_2S heterostructure. Such an elaborate reaction process changes the original coordination mode of Co nodes via the chemical valence mismatch between $Co^{2+/3+}$ and Ag^+, and reassemble coordination bonds of Ag/Ag_2S heterostructure with abundant lattice defects and vacancy sites. Meanwhile, the cation exchange is more capable of adjusting the pore size from micropore to macropore, achieving efficient mass transport as well as sufficiently exposed active surfaces in the porous framework. More importantly, the nonequivalent cation exchange mode provides a unique confinement framework for in-situ

growth of metallic Ag along with Ag_2S rich edge sites, which achieves S-vacancies and strain simultaneously by precisely regulating the initial Ag^+ ions concentration. By virtue of these structural and compositional advantages, the as-prepared 3D porous Ag/Ag_2S heterostructure exhibit remarkable catalytic performance for the HER. Theoretical calculations have unraveled the electroactivity of the interfacial regions in the Ag/Ag_2S heterostructure, which guarantees efficient electron transfer and alleviates the overbinding effect of protons. The optimized electronic structures by both surface defects and Ag cluster determine the superior HER performances of the Ag/Ag_2S heterostructure. Therefore, we expect that the nonequivalent cation exchange modulator-induced strategy would provide new insights into the preparation of hierarchically large-pore micro/nanomaterials with different compositions and functionalities.

Supporting Information
Supporting Information is available from the Wiley Online Library or from the author.

Acknowledgements

This work was financially supported by the National Natural Science Foundation of China (Project 21931001, 21871121, 21771156), Natural Science Foundation of Anhui Province (1908085MB44), Natural Science Foundation of Higher Education Institutions in Anhui province (KJ2019A0524, KJ2020A0541), the Natural Science Foundation of Fuyang Normal College (2019KYQD0019), the Innovation Training Program for the College Students (202010371002), the 111 Project (B20027) and the Early Career Scheme (ECS) fund (Grant No.: PolyU 253026/16P) from the Research Grant Council (RGC) in Hong Kong.

Received: ((will be filled in by the editorial staff))
Revised: ((will be filled in by the editorial staff))
Published online: ((will be filled in by the editorial staff))

References

[1] C. M. A. Parlett, K. Wilson and A. F. Lee, *Chem. Soc. Rev.*, 2013, **42**, 3876-3893.

[2] P. Horcajada, T. Chalati, C. Serre, B. Gillet, C. Sebrie, T. Baati, J. F. Eubank, D. Heurtaux, P. Clayette, C. Kreuz, J.-S. Chang, Y. K. Hwang, V. Marsaud, P.-N. Bories, L. Cynober, S. Gil, G. Férey, P. Couvreur and R. Gref, *Nat Mater*, 2009, **9**, 172.

[3] H. Wang, X. Wang, M. Li, L. Zheng, D. Guan, X. Huang, J. Xu and J. Yu, *Adv. Mater.*, 2020,**32**, 2002559.

[4] H. Chen, X. Liang, Y. Liu, X. Ai, T. Asefa and X. Zou, *Adv. Mater.*, 2020, **32**, 2002435.

[5] H. Zhang, W. Zhou, J. Dong, X. F. Lu and X. W. Lou, *Energy Environ. Sci,* 2019, **12**, 3348-3355.

[6] G. Chen, Y. Yan, J. Wang, Y. S. Ok, G. Zhong, B. Y. Guan and Y. Yamauchi, *Angew. Chem. Int. Ed.*, 2020, **59**, 19663-19668.

[7] R. Miao, B. Dutta, S. Sahoo, J. He, W. Zhong, S. A. Cetegen, T. Jiang, S. P. Alpay and S. L. Suib, *J Am Chem Soc*, 2017, **139**, 13604-13607.

[8] M. Qiao, Y. Wang, Q. Wang, G. Hu, X. Mamat, S. Zhang and S. Wang, *Angew. Chem. Int. Ed.*, 2020, **59**, 2688-2694.

[9] L. Yang, X. Zeng, W. Wang and D. Cao, *Adv. Funct. Mater.*, 2018, **28**, 1704537.

[10] B. Y. Guan, X. Y. Yu, H. B. Wu and X. W. Lou, *Adv. Mater.*, 2017, **29**, 1703614.

[11] H. Xu, C. Shan, X. Wu, M. Sun, B. Huang, Y. Tang and C.-H. Yan, *Energy Environ. Sci*, 2020, **13**, 2949-2956.

[12] Z.-X. Cai, Z.-L. Wang, J. Kim and Y. Yamauchi, *Adv. Mater.*, 2019, **31**, 1804903.

[13] H. Liu, J. Guan, S. Yang, Y. Yu, R. Shao, Z. Zhang, M. Dou, F. Wang and Q. Xu, *Adv. Mater.*, 2020, **32**, 2003649.

[14] Z. Ye, Y. Jiang, L. Li, F. Wu and R. Chen, *Adv. Mater.*, 2020, **32**, 2002168.

[15] H. Xu, J. Cao, C. Shan, B. Wang, P. Xi, W. Liu and Y. Tang, *Angew. Chem. Int. Ed.*, 2018, **57**, 8654-8658.

[16] J. Lai, B. Huang, Y. Chao, X. Chen and S. Guo, *Adv. Mater.*, 2019, **31**, 1805541.

[17] T. Liu, P. Li, N. Yao, G. Cheng, S. Chen, W. Luo and Y. Yin, *Angew. Chem. Int. Ed.*, 2019, **58**, 4679-4684.

[18] W. He, I. Liberman, I. Rozenberg, R. Ifraemov and I. Hod, *Angew. Chem. Int. Ed.*, 2020, **59**, 8262-8269.

[19] B. Sadtler, D. O. Demchenko, H. Zheng, S. M. Hughes, M. G. Merkle, U. Dahmen, L.-W. Wang and A. P. Alivisatos, *J Am Chem Soc*, 2009, **131**, 5285-5293.

[20] J. L. Fenton, B. C. Steimle and R. E. Schaak, *Science*, 2018, **360**, 513-517.

[21] Y. Fang, D. Luan, Y. Chen, S. Gao and X. W. D. Lou, *Angew. Chem. Int. Ed.*, 2020, **59**, 2644-2648.

[22] S.-C. Qi, X.-Y. Qian, Q.-X. He, K.-J. Miao, Y. Jiang, P. Tan, X.-Q. Liu and L.-B. Sun, *Angew. Chem. Int. Ed.*, 2019, **58**, 10104-10109.

[23] H. Zhou, Y. Zhao, J. Gan, J. Xu, Y. Wang, H. Lv, S. Fang, Z. Wang, Z. Deng, X. Wang, P. Liu, W. Guo, B. Mao, H. Wang, T. Yao, X. Hong, S. Wei, X. Duan, J. Luo and Y. Wu, *J Am Chem Soc*, 2020, **142**, 12643-12650.

[24] M. Pang, J. Hu and H. C. Zeng, *J Am Chem Soc*, 2010, **132**, 10771-10785.

[25] J. B. Rivest and P. K. Jain, *Chem. Soc. Rev.*, 2013, **42**, 89-96.

[26] L. De Trizio, R. Gaspari, G. Bertoni, I. Kriegel, L. Moretti, F. Scotognella, L. Maserati, Y. Zhang, G. C. Messina, M. Prato, S. Marras, A. Cavalli and L. Manna, *Chem Mater*, 2015, **27**, 1120-1128.

[27] Y. Yin, J. Han, Y. Zhang, X. Zhang, P. Xu, Q. Yuan, L. Samad, X. Wang, Y. Wang, Z. Zhang, P. Zhang, X. Cao, B. Song and S. Jin, *J Am Chem Soc*, 2016, **138**, 7965-7972.

[28] L. Li, Z. Qin, L. Ries, S. Hong, T. Michel, J. Yang, C. Salameh, M. Bechelany, P. Miele, D. Kaplan, M. Chhowalla and D. Voiry, *ACS Nano*, 2019, **13**, 6824-6834.

[29] L. Oakes, R. Carter, T. Hanken, A. P. Cohn, K. Share, B. Schmidt and C. L. Pint, *Nat. Commun.*, 2016, **7**, 11796.

[30] D. Voiry, H. Yamaguchi, J. Li, R. Silva, D. C. B. Alves, T. Fujita, M. Chen, T. Asefa, V. B. Shenoy, G. Eda and M. Chhowalla, *Nat Mater*, 2013, **12**, 850.

[31] C. Chen, Y. Kang, Z. Huo, Z. Zhu, W. Huang, H. L. Xin, J. D. Snyder, D. Li, J. A. Herron, M. Mavrikakis, M. Chi, K. L. More, Y. Li, N. M. Markovic, G. A. Somorjai, P. Yang and V. R. Stamenkovic, *Science*, 2014, **343**, 1339-1343.

[32] X. Du, J. Huang, J. Zhang, Y. Yan, C. Wu, Y. Hu, C. Yan, T. Lei, W. Chen, C. Fan and J. Xiong, *Angew. Chem. Int. Ed.*, 2019, **58**, 4484-4502.

[33] B. You, M. T. Tang, C. Tsai, F. Abild-Pedersen, X. Zheng and H. Li, *Adv. Mater.*, 2019, **31**, 1807001.

[34] M. Motlag, P. Kumar, K. Y. Hu, S. Jin, J. Li, J. Shao, X. Yi, Y.-H. Lin, J. C. Walrath, L. Tong, X. Huang, R. S. Goldman, L. Ye and G. J. Cheng, *Adv. Mater.*, 2019, **31**, 1900597.

[35] S. M. Lee, W. Jang, B. C. Mohanty, J. Yoo, J. W. Jang, D. B. Kim, Y. Yi, A. Soon and Y. S. Cho, *Chem Mater*, 2018, **30**, 7776-7781.

[36] J. Miao, Z. Xu, Q. Li, A. Bowman, S. Zhang, W. Hu, Z. Zhou and C. Wang, *ACS Nano*, 2017, **11**, 10472-10479.

[37] W. Han, Z. Liu, Y. Pan, G. Guo, J. Zou, Y. Xia, Z. Peng, W. Li and A. Dong, *Adv Mater*, 2020, **32**, e2002584.

[38] H. Li, C. Tsai, A. L. Koh, L. Cai, A. W. Contryman, A. H. Fragapane, J. Zhao, H. S. Han, H. C. Manoharan, F. Abild-Pedersen, J. K. Nørskov and X. Zheng, *Nat Mater*, 2015, **15**, 48.

[39] H. Zhu, G. Gao, M. Du, J. Zhou, K. Wang, W. Wu, X. Chen, Y. Li, P. Ma, W. Dong, F. Duan, M. Chen, G. Wu, J. Wu, H. Yang and S. Guo, *Adv. Mater.*, 2018, **30**, 1707301.

[40] Z. Tian, C. Song, C. Wang, H. Xu and Q. Guan, *J Nanopart Res*, 2020, **22**, 161.

[41] J. Yin, J. Jin, H. Lin, Z. Yin, J. Li, M. Lu, L. Guo, P. Xi, Y. Tang and C. H. Yan, *Adv. Sci.*, 2020, **7**, 1903070.

[42] X. Wang, Y. Zhang, H. Si, Q. Zhang, J. Wu, L. Gao, X. Wei, Y. Sun, Q. Liao, Z. Zhang, K. Ammarah, L. Gu, Z. Kang and Y. Zhang, *J Am Chem Soc*, 2020, **142**, 4298-4308.

[43] J. R. Petrie, H. Jeen, S. C. Barron, T. L. Meyer and H. N. Lee, *J Am Chem Soc*, 2016, **138**, 7252-7255.

In this work, we develop an effective nonequivalent cation exchange strategy for engineering the hierarchically porous Ag/Ag_2S heterostructure, which has shown superior catalytic performance for hydrogen evolution reaction (HER). The heterostructure guarantees efficient electron transfer and alleviates the overbinding effect of protons, leading to low overpotential of HER and long-term stability in the acidic media.

H. Xu, X. Niu, Z. Liu, M. Sun, Z. Liu, Z. Tian, X. Wu, B. Huang, Y. Tang, and C.-H.Yan

Title Hierarchically Porous Ag/Ag2S Heterostructure by Cation Exchange for Efficient Hydrogen Evolution